Pergamon

SHOCK SYNTHESIS OF SILICIDES—I. EXPERIMENTATION AND MICROSTRUCTURAL EVOLUTION

K. S. VECCHIO, LI-HSING YU and M. A. MEYERS

Department of Applied Mechanics and Engineering Sciences, University of California, San Diego,
La Jolla, CA 92093-0411, U.S.A.

Abstract—Niobium and molybdenum silicides were synthesized by the passage of high-amplitude shock waves through elemental powder mixtures. These shock waves were generated by planar parallel impact of explosively-accelerated flyer plates on momentum-trapped capsules containing the powders. Recovery of the specimens revealed unreacted, partially-reacted, and fully-reacted regions, in accord with shock energy levels experienced by the powder. Electron microscopy was employed to characterize the partially- and fully-reacted regions for the Mo–Si and Nb–Si systems, and revealed only equilibrium phases. Selected-area and convergent beam electron diffraction combined with X-ray microanalysis verified the crystal structure and compositions of the reacted products. Diffusion couples between Nb and Si were fabricated for the purpose of measuring static diffusion rates and determining the phases produced under non-shock condition. Comparison of these non-shock diffusion results with the shock synthesis results indicates that a new mechanism is responsible for the production of the $NbSi_2$ and $MoSi_2$ phases under shock compression. At the local level the reaction can be rationalized, for example, in the Nb–Si system under shock compression, through the production of a liquid-phase reaction product ($NbSi_2$) at the Nb-particle/Si-liquid interface, the formation of spherical nodules ($\sim 2 \mu m$ diameter) of this product through interfacial tension, and their subsequent solidification.

1. INTRODUCTION

Shock-induced reactions (or shock synthesis) have been studied since the 1960s but are still poorly understood, partly due to the fact that the reaction kinetics are very fast making experimental analysis of the reaction difficult. Shock-induced reactions are quite distinct from shock-induced phase transformations, such as the synthesis of diamond from graphite which is a diffusionless phase transformation. Shock-induced reactions also differ from detonations because only condensed products are formed, in the former. Shock synthesis is closely related to combustion synthesis, and occurs in the same systems that undergo exothermic gasless combustion reactions. The thermite reaction ($Fe_2O_3 + 2Al \rightarrow 2Fe + Al_2O_3$) is prototypical of this class of reactions. The first report of these shock-induced reactions is due to Batsanov et al. [1]. This initial discovery was followed by activity in Japan [2, 3] and the USSR [4–8]. In the U.S., the pioneering work of Graham and co-workers [9–11] was followed by investigations by Vreeland and co-workers [12, 13], Horie et al. [14, 15], Boslough [16], Thadhani and co-workers [17, 18], and Yu et al. [19, 20].

Shock-wave propagation through materials generates significant structural changes; these effects have been the object of extensive studies, that were initiated with the Manhattan project in the 1940's and continue to this day. Analytical investigations coupled with experimental studies have yielded mechanisms rationalizing the production of dislocations and point defects due to shock-wave passage through solid materials. The first mechanism was proposed by Smith [21], followed by Hornbogen [22] and later modified by Meyers [23], and Weertman [24]. The effects of shock-wave passage through porous (powder) materials are considerably more complex, because intense and non-uniform plastic deformation is coupled with the shock-wave effects. Thus, the particle interiors experience primarily the effects of shock waves, while the surfaces undergo intense plastic deformation which can often result in interfacial melting. This localized melting leads to the bonding of the powder, and this gave rise to the research field of shock-wave compaction. Quantitative, predictive models have been developed by Gourdin [25] and Schwarz et al. [26].

Shock synthesis of compounds from powders is triggered by the extraordinarily high energy deposition rate at the surfaces of the powders, thereby changing their configuration, forcing them in close contact, activating them by introducing large densities of defects, and heating them close to or even above their melting temperatures [8–11]. Some fundamental questions regarding these reactions remain unanswered. Prominent among them are the following: (1) How can the extraordinarily high reaction rates encountered in shock compression be explained?

(2) Are the phases formed under shock-synthesis conditions unique and/or non-equilibrium?

This paper (in conjunction with its companion paper [27]) presents experimental results coupled with characterization and analysis of two metal silicides formed by shock synthesis directed at providing an answer to these questions. It is shown that the mechanism of shock-induced reaction is quite different than conventional solid-state reaction mechanisms for the silicides. The high thermal gradients imparted by the effect of shock compression, combined with the high pressures and material flux, enable a reaction mechanism unique to shock compression; however, only equilibrium phases and structures were found for the systems investigated.

2. EXPERIMENTAL PROCEDURES

Two elemental powder mixtures were used in this investigation: Nb–Si and Mo–Si. The powders, produced by CERAC, had irregular shapes, and sizes smaller than 44 μm (-325 mesh). The purity levels were 99.9% for Nb, Mo and Si. The powders were mixed in the proportions to provide, upon reaction, the intermetallic compounds $NbSi_2$ and $MoSi_2$, for each system respectively. These powders were encapsulated under controlled argon atmosphere in stainless steel capsules (internal dimensions of 15 mm diameter and 5 mm height). These capsules were subjected to shock compression in a Sawaoka fixture; this fixture is described in detail elsewhere [e.g. 28]; the system (cross-section) is shown in Fig. 1. Each system contains 12 capsules; four sectioned capsules are shown in this figure. A flyer plate is accelerated downwards by an explosive system consisting of a main charge (PBX 9404 explosive) initiated simultaneously along its top surface by an explosive lens consisting of two explosives with different detonation velocities. Impact velocities of 1.2 and 1.9 km/s were achieved by varying the quantity and type of explosive accelerating the flyer plate. Shock experiments were conducted on capsules at room temperature and others preheated to 773 K.

The high-temperature shock fixture is shown in Fig. 1(b). The capsules and momentum traps are heated in a discardable furnace, with the explosive system at a safe distance. When the temperature reaches the desired value, the furnace top is removed and the explosive assembly, together with the flyer plate, roll down a 4° inclined ramp until they are properly positioned above the capsule; the system is then electrically detonated. Solenoid 1 ensured remote activation and enabled the flyer plate/explosive system to roll down at the desired time. In case of misfire or any other unexpected event, the explosive system could be withdrawn from above the furnace by the activation of solenoid 2.

After shock processing, the specimen capsules were sectioned and analyzed by scanning and transmission electron microscopy. Scanning electron microscopy

(SEM) was conducted on a Cambridge S360 electron microscope equipped with a LINK Analytical energy dispersive X-ray spectrometer (EDS). Compositional measurements of individual phases were conducted using the ZAF correction procedure with unreacted powder regions used for standards. Since the shock experiment is very rapid, and the resultant thermal excursion short lived, the unreacted powder regions were considered chemically unchanged and subsequently used as pure elemental standards. Standardless quantification was also conducted on both the unreacted powders, and the reaction products,
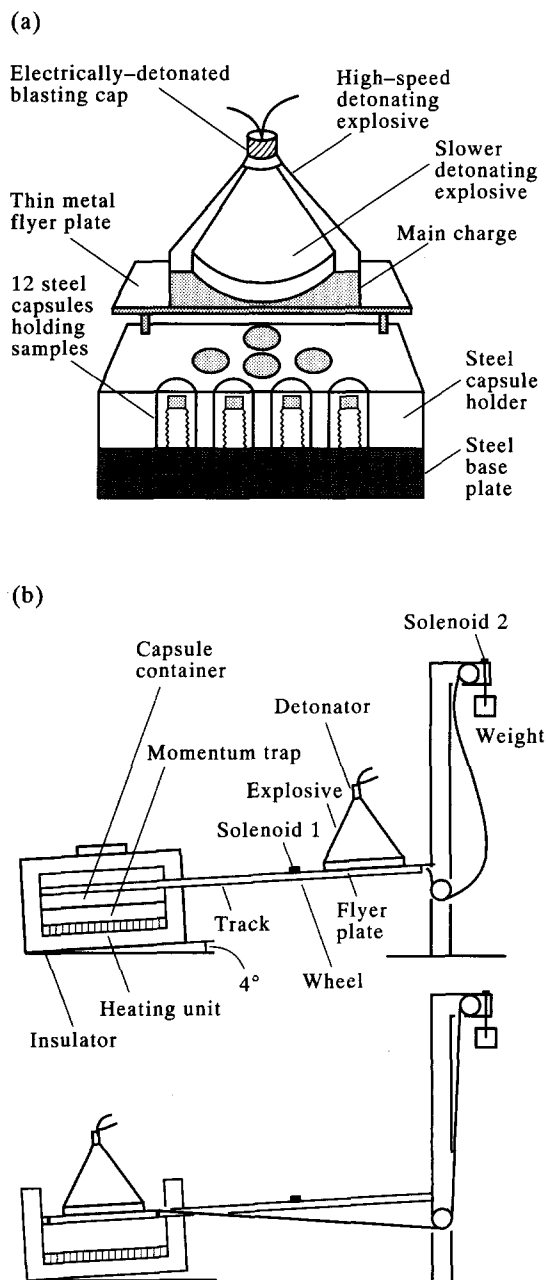
(a)

(b)

Fig. 1. Schematic illustration of planar impact (Sawaoka) system: (a) room temperature fixture, (b) elevated temperature shock fixture.

and the results were consistent with the standards-based quantification results.

Static reaction experiments (i.e. non-shock experiments) were conducted by annealing Nb–Si diffusion couples for different times at 1200°C and recovering the specimens for observation. The identification of reaction products and their thicknesses in these diffusion couples was established by SEM and quantitative EDS X-ray microanalysis using the specimen regions well away from the interface as pure elemental standards.

Transmission electron microscopy (TEM) was carried out in a Philips CM30 electron microscope equipped with a LINK Analytical AN1085 ultra-thin window (UTW) energy dispersive X-ray spectrometer (EDS) system. The TEM work was conducted at an accelerating voltage of 300 kV, with the exception of both the X-ray microanalysis and convergent beam electron diffraction work which were each conducted at 100 kV.

The pressure and temperatures induced by shock waves in the capsules were obtained from computer simulations, conducted by Norwood and Graham [29]. Two-dimensional effects are very important since the shock waves travel faster in the capsule than in the powder. Thus, the shock waves enter the capsules laterally, as well as at their top surface, generating highly inhomogeneous pressure and temperature regimes. This inhomogeneity in both pressures and temperatures was readily apparent within the recovered capsules, and was actually a highly useful effect since it enabled the analysis of unreacted, partially-reacted, and fully-reacted regions within the same specimen.

3. EXPERIMENTAL RESULTS AND DISCUSSION

3.1. Shock recovery experiments

Figure 2 shows reaction maps of the cross-sections for the recovered capsules for the Nb–Si and Mo–Si samples; fully-reacted, partially-reacted, and unreacted regions are evident. Upon recovery, the specimens were considerably cracked, and portions of the specimens were lost during sectioning.
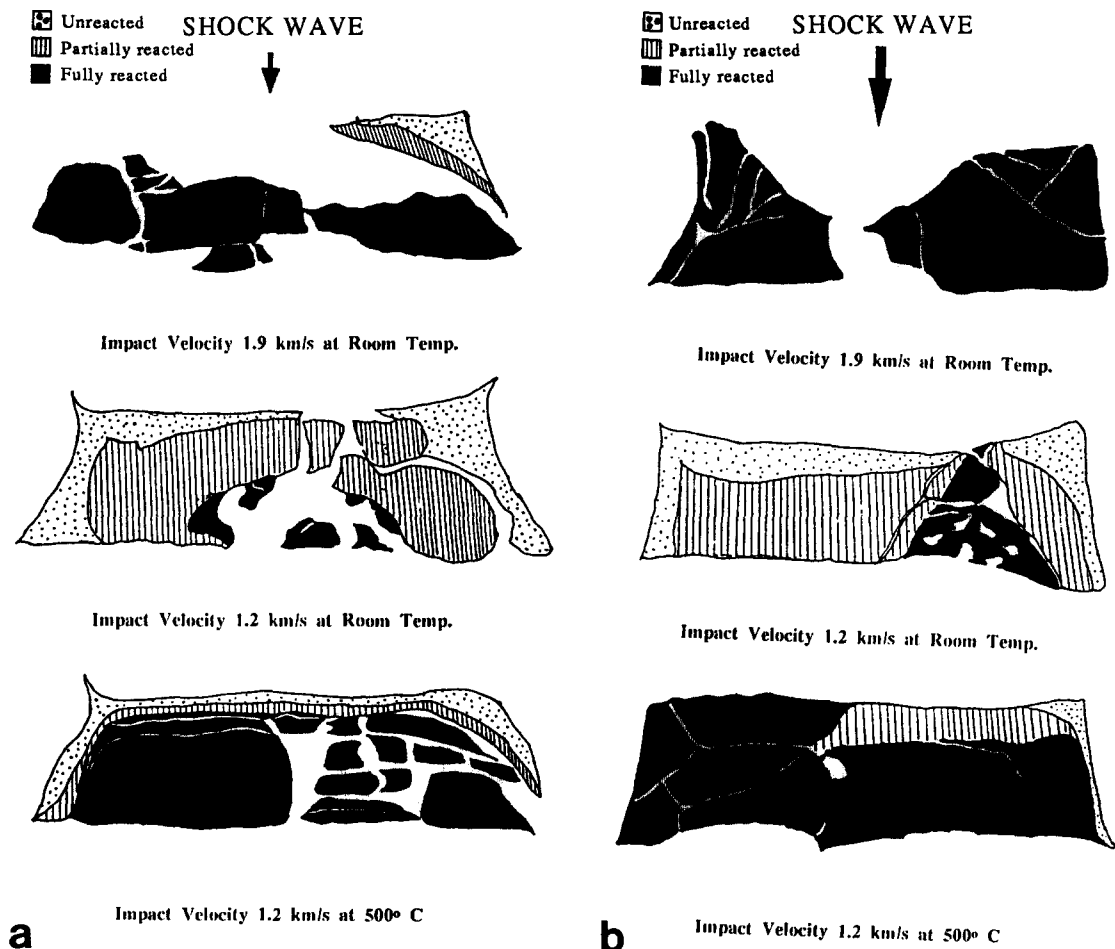

Fig. 2. Maps showing fully-reacted, partially-reacted, and unreacted regions for (a) Nb–Si system and (b) Mo–Si system. Impact velocity and temperature marked below each plot. Black regions represent fully-reacted, hatched regions-partially-reacted, dotted region-unreacted, and white represents voids and/or cracks.

3.1.1. Scanning electron microscopy and micro-analysis. Backscattered electron micrographs of a polished section of the Nb–Si sample shocked at room temperature and low velocity (1.2 km/s) are shown in Fig. 3. Figure 3(a) shows the unreacted but compacted region taken from near the top of the capsule. Figure 3(b) shows the transition region between unreacted and partially-reacted material, with the reacted material being the small gray nodules identified as $NbSi_2$ (Nb–38 wt% Si via X-ray micro-analysis); the identification of the crystal structure of this phase will be discussed in detail later. Figure 3(c) shows the partially-reacted region which made up the majority of the sample and consisted of Nb particles surrounded by a reaction layer of $NbSi_2$ nodules and embedded within a two-phase matrix of $NbSi_2$ nodules and silicon. Figure 3(d) shows the transition region from the partially-reacted to fully-reacted material located near the bottom of the capsule. Within this transition region an additional interfacial
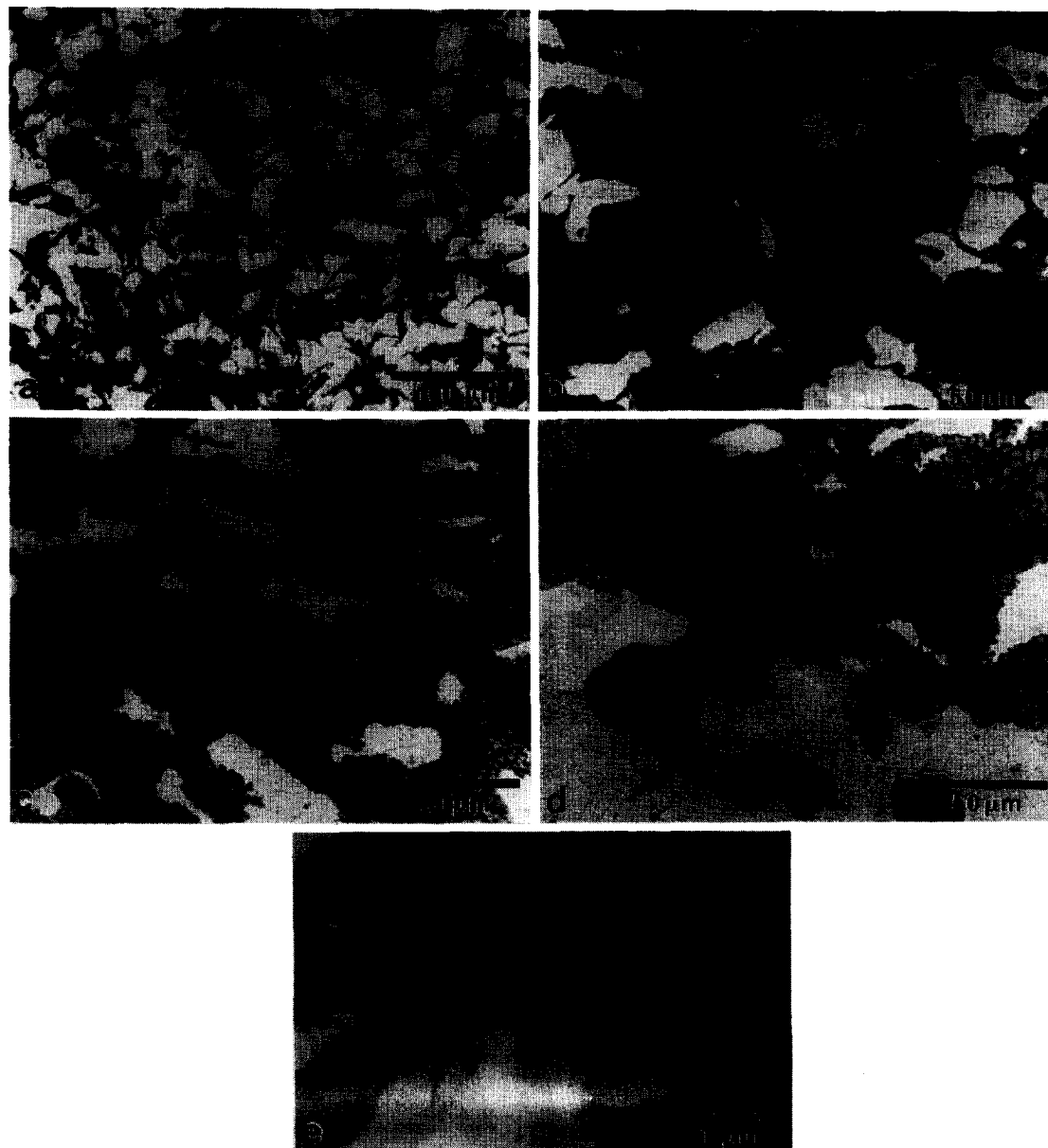

Fig. 3. Backscattered electron micrographs of (a) the unreacted but compacted region taken from near the top of the capsule, (b) the transition region between unreacted and partially-reacted material, with the reacted material being the small gray nodules identified as $NbSi_2$, (c) the partially-reacted region which makes up the majority of the sample and consists of Nb particles surrounded by a reaction layer of $NbSi_2$ nodules and embedded within a two-phase matrix of $NbSi_2$ nodules and silicon, (d) the transition region from the partially-reacted to fully-reacted material located near the bottom of the capsule; within this transition region an addition interfacial reaction product could be observed as shown in (e) which was identified by X-ray microanalysis as Nb_5Si_3.

reaction product could be observed as shown in Fig. 3(e) which was identified by X-ray microanalysis as Nb_5Si_3 (Nb–15 wt% Si). Some Nb_5Si_3 reaction product could be found between the $NbSi_2$ phase and the Nb particles within the partially-reacted region; however, the thickness of the Nb_5Si_3 layer, in this region, never exceeded 100 nm. In the transition region, the Nb_5Si_3 layer exceeded 1 μm in thickness. In the unreacted region, the niobium particles retain their original powder configuration (i.e. undeformed, irregularly shaped particles), whereas the silicon particles have been deformed and compacted around the
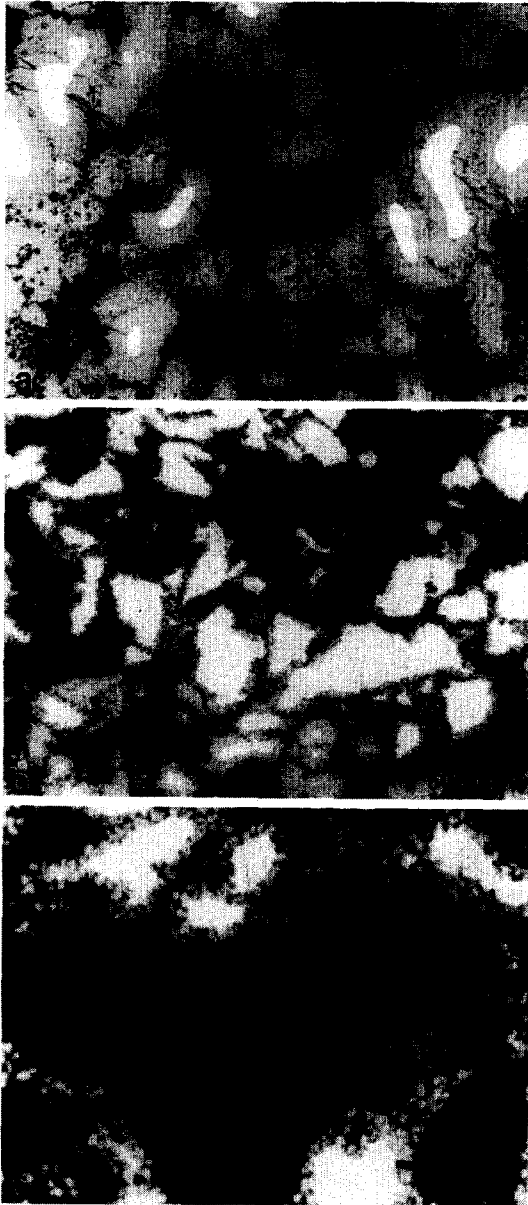

Fig. 4. Backscattered electron micrographs of the microstructure of (a) the partially-reacted region in the low velocity (1.2 km/s) and elevated temperature (773 K) shock experiment, (b, c) the partially-reacted region of the specimen shocked at higher velocity (1.9 km/s) and room temperature.

niobium particles. Figure 4(a) shows a backscattered electron micrograph of the microstructure of the partially-reacted region in the low velocity (1.2 km/s) and elevated temperature (773 K) shock experiment. The most notable feature that differentiates this sample from the room temperature, low velocity experiment is the significantly increased amount of reacted product $NbSi_2$. Comparison between Fig. 3(c) and Fig. 4(a) indicates that a greater volume fraction of $NbSi_2$ was formed as a result of capsule preheating. This is expected since a higher temperature will be achieved in the capsule as a result of the shock, plus preheating, and the capsule will remain hotter for a longer time following the shock since the shock fixture is no longer an efficient quenching medium.

Figure 4(b, c) show the partially-reacted region of the specimen shocked at higher velocity (1.9 km/s) and room temperature. In this sample less nodular $NbSi_2$ was observed; however, a significant amount of $NbSi_2$ was also found present as a lamellar eutectic structure within the silicon rich matrix, as shown in Fig. 4(c). Under these shock conditions, the molten silicon matrix becomes enriched with niobium, and subsequently solidifies at 1300°C via a eutectic reaction between Si and $NbSi_2$. A small amount of this eutectic reaction was evident in the other two Nb–Si samples; however, in those samples the volume fraction was very insignificant compared to the amount of nodular $NbSi_2$ that was found.

This result suggests that the temperature throughout the molten Si exceeded the melting temperature of the $NbSi_2$ phase ($\sim$ 1940°C) causing the nodular $NbSi_2$ to dissolve in Si and to subsequently resolidify through the eutectic reaction. Incontrovertible proof that silicon was molten in the partially-reacted region of even the low velocity, room temperature experiment is provided by the observation of a fine eutectic structure of lamellar $NbSi_2$ and Si. This eutectic structure formed last as the molten, Nb-enriched silicon solidified. The higher shock energies achieved in the 1.9 km/s sample result in significantly higher temperatures within the powders. A greater fraction of this shock energy is deposited in the silicon powder compared to the Nb powder as evidenced by the considerable plastic deformation of the silicon particles in the unreacted region, and the extremely high temperature achieved in the molten silicon in the partially-reacted region. In addition, the higher shock energy is likely to result in increased turbulence in the molten Si which will aid in homogenizing the melt (i.e. dissolve the $NbSi_2$ nodules) through a stirring action. Clearly, the reaction mechanism associated with the formation of the nodular $NbSi_2$ is distinct from the eutectic reaction observed in Fig. 4(b, c).

Comparison of the low velocity (1.2 km/s), elevated temperature (773 K) experiment with the room temperature, high velocity (1.9 km/s) experiment reveals several interesting observations regarding the nature and extent of the shock reaction. First, the extent of reaction (i.e. the amount of reaction product formed)

was greater for the low velocity (1.2 km/s), elevated temperature experiment than the high velocity (1.9 km/s) experiment, even though the high velocity experiment creates a higher temperature within the capsule compared to the low velocity, elevated temperature experiment after the preheat temperature is added to the calculated temperatures (as based on the calculations of Norwood and Graham [29] also shown as Fig. 2 in the companion paper to this work [27]). The preheating is more effective for promoting the reaction because the temperature is uniform throughout the powders, heating up both the Nb and Si particles relatively evenly, whereas the shock energy (i.e. heat) is preferentially deposited in the softer Si particles. As such, a larger fraction of shock energy can contribute to the reaction in the preheated sample, rather than heating of the powders in the high velocity experiment. Secondly, the morphology of the NbSi$_2$ phase differs between the high velocity experiment and the elevated temperature experiment. In the high velocity experiment the NbSi$_2$ exists both as a lamellar eutectic structure within the Si regions, as well as nodules along the Nb–Si interface. In contrast, the NbSi$_2$ phase exists as nodules surrounding a thick layer of NbSi$_2$ which encapsulates the Nb particles, as shown in Fig. 4(a). Since the preheating raises the temperature of both the powders and the whole fixture itself, the cooling rate in this experiment is considerably lower than in either of the other two (low velocity–room temperature and high velocity–room temperature) experiments. The morphology of the thick NbSi$_2$ reaction layer surrounding the Nb particles suggests that this layer: (1) forms through solid-state diffusion, (2) occurs subsequent to the nodule reaction mechanism, and (3) is not directly associated with shock-wave passage.

Backscattered electron micrographs of a polished section of the Mo–Si sample shocked at room temperature and low velocity (1.2 km/s) are shown in Fig. 5. Analysis of the other two Mo–Si samples will not be presented here, but examination of these samples revealed structures similar to the corresponding Nb–Si samples. Figure 5(a) shows the unreacted but compacted region taken from near the top of the capsule. Figure 5(b) shows the transition region between unreacted and partially-reacted material, with the reacted material being the small gray nodules
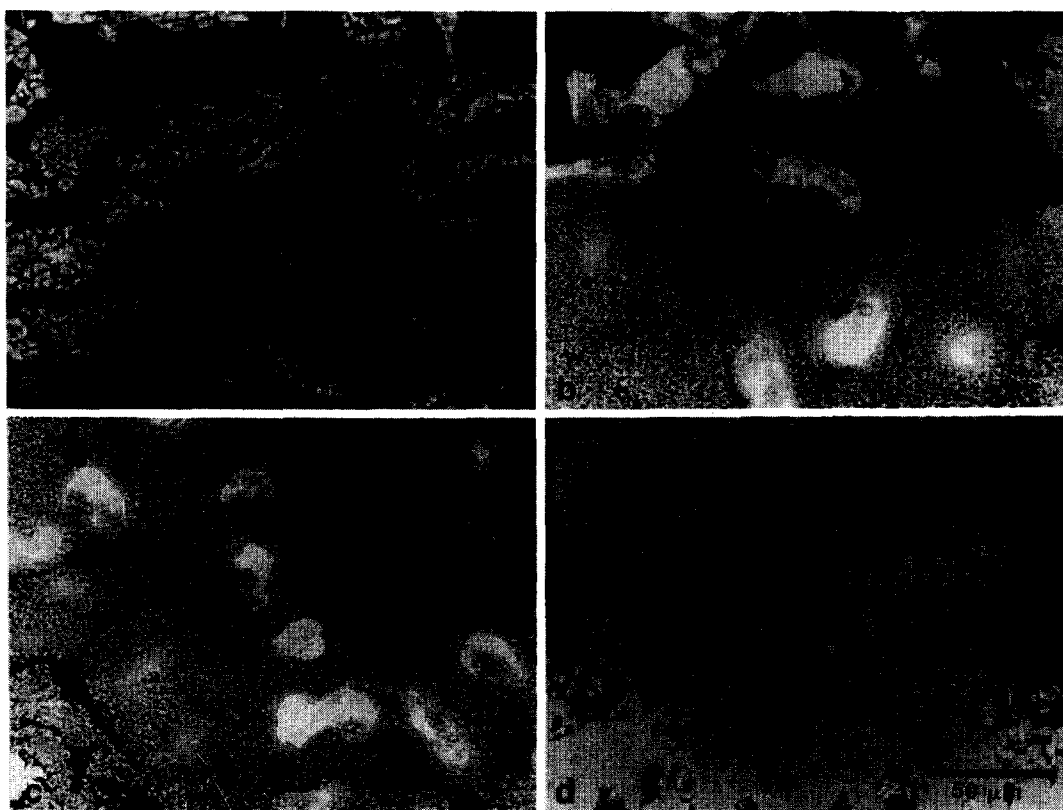

Fig. 5. Backscattered electron micrographs of a polished section of the Mo–Si sample shocked at room temperature and low velocity (1.2 km/s), (a) the unreacted but compacted region taken from near the top of the capsule, (b) the transition region between unreacted and partially-reacted material, with the reacted material being the small gray nodules identified as MoSi$_2$, (c) the partially-reacted region which made up the majority of the sample and consisted of Mo particles surrounded by a reaction layer of MoSi$_2$ nodules and embedded within a two-phase matrix of MoSi$_2$ nodules and silicon; in many instances, the entire Mo particle has been reacted to form the MoSi$_2$ phase, as indicated by an arrow in (c); (d) shows the transition region from the partially-reacted to fully-reacted material located near the bottom of the capsule.

identified as $MoSi_2$ (Mo–37 wt% Si via X-ray micro-analysis); the identification of the crystal structure of this phase will be presented later. Figure 5(c) shows the partially-reacted region which made up the majority of the sample and consisted of Mo particles surrounded by a reaction layer of $MoSi_2$ nodules and embedded within a two-phase matrix of $MoSi_2$ nodules and silicon. In many instances, the entire Mo particle has been reacted to form the $MoSi_2$ phase, as indicated by an arrow in Fig. 5(c). Figure 5(d) shows the transition region from the partially-reacted to fully-reacted material located near the bottom of the capsule. No additional interfacial reaction product could be observed in this sample, unlike the Nb–Si samples. In the unreacted region, the Mo particles appear to fragment along grain boundaries within the particles, while the silicon particles seem to have undergone intense plastic deformation.

The fully-reacted regions for the Nb–Si and Mo–Si samples were essentially identical in term of macroscopic morphology. Voids were present throughout, resulting from either solidification shrinkage, gases evolved during the reaction, or tensile stresses imposed on the compact prior to solidification. The presence of spherical voids, as well as dendritic structures observed are evidence of melting and

Fig. 7. (a) Backscattered electron micrograph of the fully-reacted region of the Mo–Si capsule which contains primarily $MoSi_2$ [labeled A in this figure]; (b) shows a typical EDS spectrum from this phase. A second phase [labeled B in (a)] had a composition close to Mo_5Si_3, but also contained small amounts of Fe, Cr and Ni, as shown in the EDS spectrum of (c).
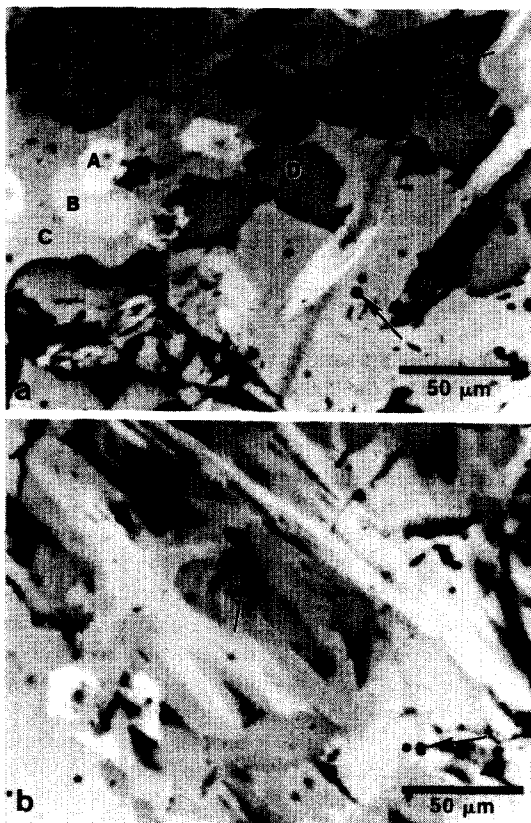

Fig. 6. Backscattered electron micrographs of fully-reacted regions of the Nb–Si capsules tested at (a) elevated temperature (773 K) and (b) high velocity (1.9 km/s) and room temperature. Microvoids are marked by arrows and several different phases are present marked A, B, C and D in (a).
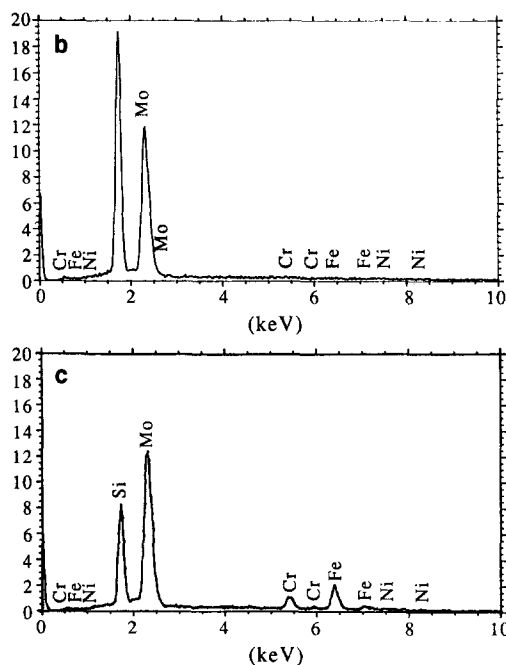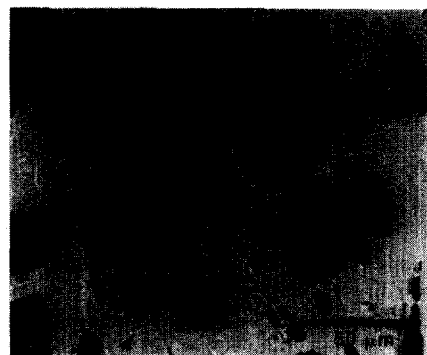
re-solidification. Figure 6(a) and (b) show the microstructure in the fully-reacted regions of the Nb–Si capsules tested at elevated temperature (773 K) and high velocity (1.9 km/s), respectively; the microvoids are marked by arrows and several different phases are present. Energy dispersive X-ray analysis of these distinct phases [marked A, B, C and D in Fig. 6(a) for example] reveals Fe, Ni and Cr peaks, in addition to differences in the relative intensities of the much larger Nb and Si peaks. The presence of Fe, Ni and Cr is evidence for melting of the capsule (which is stainless steel) and subsequent contamination of specimen. This is a post-shock effect, since there would be no time for diffusion of these elements during shock-wave passage. The phases which contained the Fe, Cr and Ni to varying amounts also had an overall Nb–Si ratio close to the composition of Nb_5Si_3. Figure 7(a) shows the fully-reacted region of the Mo–Si capsule

which contains primarily $MoSi_2$ [labeled A in this figure]; Fig. 7(b) shows a typical EDS spectrum from this phase. A second phase [labeled B in Fig. 7(a)] had a composition close to Mo_5Si_3, but also contained small amounts of Fe, Cr and Ni, as shown in the EDS spectrum of Fig. 7(c). This result, in conjunction with similar findings for the Nb–Si system suggest that the Nb_5Si_3 and Mo_5Si_3 phases have a greater solubility for Fe, Cr, and Ni compared to the corresponding disilicide phases.

3.1.2. Transmission electron microscopy and diffraction analysis. Figure 8 shows transmission electron micrographs of the partially-reacted region of the low impact velocity, room temperature Nb–Si

Fig. 8. Transmission electron micrographs of the partially-reacted region of the low velocity, room temperature Nb–Si sample. (a, b) reveal the structure of the nodules and of the surrounding silicon matrix. The silicon surrounding these reacted regions generally shows an annealed structure with a profusion of annealing twins. (c) Electron diffraction pattern from twins in (b).
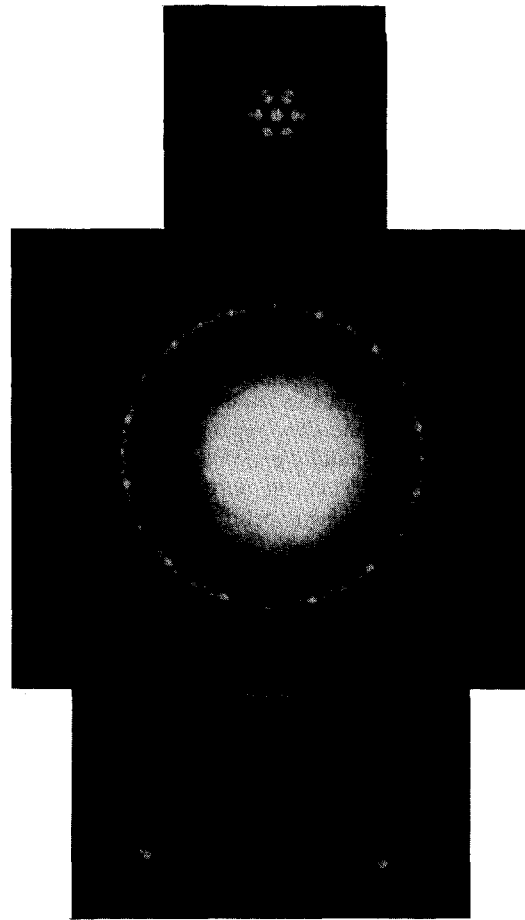

Fig. 9. [0001] zone axis CBED pattern obtained from the $NbSi_2$ nodules, (a) shows the zero-order Laue layer pattern which possesses 6 *mm* projection diffraction symmetry, (b) shows the whole pattern revealing only 6-fold rotational symmetry; no mirror planes exist in this pattern, and (c) shows an enlarged view of the black rectangle outlining a small portion of the second-order Laue ring in (b).

sample. Figure 8(a) and (b) reveal the structure of the nodules and of the surrounding silicon matrix. The $NbSi_2$ nodules are monocrystalline, approx. 1–2 μm in diameter, and have facets. They do not show any marked internal structure, such as dislocations, stacking faults, or twins. The silicon surrounding these reacted regions generally shows an annealed structure with a profusion of annealing twins, as shown in Fig. 8(b). A few silicon regions exhibit a microcrystalline structure. These regions were either subjected to intense plastic deformation and recrystallized (statically or dynamically) or were molten and rapidly re-solidified. This microstructure is in stark contrast with the previous silicon regions [Fig. 8(b)] which suggested melting followed by slow re-solidification.

The crystal structure of the $NbSi_2$ nodules was determined by convergent beam electron diffraction (CBED) analysis. Figure 9 shows the [0001] zone axis CBED pattern obtained from the $NbSi_2$ nodules. Figure 9(a) shows the zero-order Laue layer pattern

Fig. 11. Transmission electron micrograph of the partially-reacted region of the low velocity, room temperature Mo–Si sample revealing the internal structure of the $MoSi_2$ nodules including dislocations and twins.

Fig. 10. Transmission electron micrographs of the partially-reacted region of the low velocity, room temperature Mo–Si sample, (a) and (b) reveal the structure of the $MoSi_2$ nodules and the surrounding silicon matrix, respectively. The silicon surrounding these reacted regions generally shows an annealed structure with a profusion of annealing twins.

here, displayed only 2-fold whole-pattern symmetry consistent with the point group 622. The established crystal structure for the $NbSi_2$ phase is the C40 hexagonal structure (space group $P6_222$ and point group 622) [30]. No attempt was made here to determine the space group of this phase; however there is no reason to suspect any other space group.
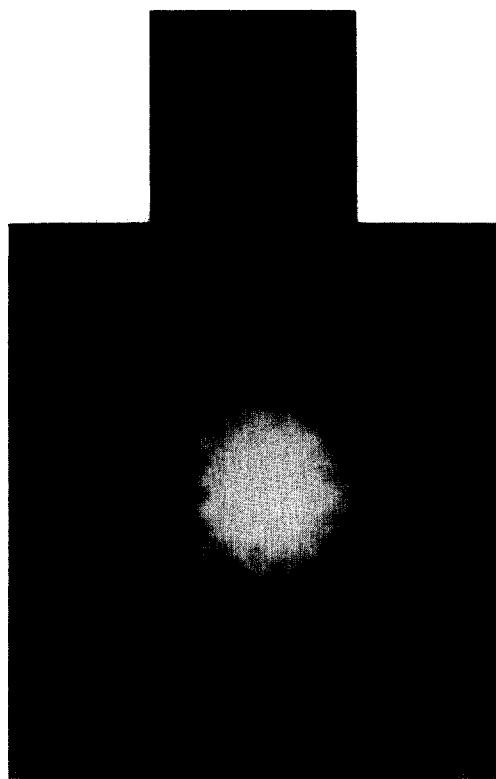
which possesses 6 *mm* projection-diffraction† symmetry. Figure 9(b) shows the whole pattern† revealing only 6-fold rotational symmetry; no mirror planes exist in this pattern. Figure 9(c) shows an enlarged view of the black rectangle outlining a small portion of the second-order Laue ring in Fig. 9(b). Careful examination of Fig. 9(c) reveals that the reflections indicated by the arrows [(7 $\overline{19}$ 12 2) and (12 $\overline{19}$ 7 2)] do not mirror to each other. This lack of mirror symmetry reduces the whole pattern symmetry from 6 *mm* to 6 in the [0001] zone axis orientation. As such, the diffraction group for this symmetry is $6m_rm_r$ and the point group is 622. CBED analysis of both the $\langle 11\overline{2}0 \rangle$ and $\langle 1\overline{1}00 \rangle$ type orientations, not shown

†The terms projection-diffraction symmetry and whole pattern symmetry have the same meanings as in Buxton et al. [31]. Projection-diffraction symmetry corresponds to the symmetry of the diffraction disks and diffuse intensity within diffraction disks of the zero-order Laue layer. Whole pattern symmetry refers to the symmetry of the higher-order Laue zone (HOLZ) reflections and HOLZ Kikuchi lines seen in low camera length patterns such as Fig. 9(b).

Fig. 12. [001] zone axis CBED pattern obtained from the $MoSi_2$ nodules, (a) shows the zero-order Laue layer pattern which possesses 4 *mm* projection-diffraction symmetry, and (b) shows the whole-pattern symmetry revealing 4 *mm* symmetry as well.

Figures 10 and 11 show transmission electron micrographs of the partially-reacted region of the low impact velocity, room temperature Mo–Si sample. Figure 10(a) and (b) reveal the structure of the MoSi$_2$ nodules and the surrounding silicon matrix, respectively. The MoSi$_2$ nodules are monocrystalline, approx. 1–2 μm in diameter, and have facets. They show significant internal structure, including dislocations and twins, as shown in Figure 11. The silicon surrounding these reacted regions generally shows an annealed structure with a profusion of annealing twins, as shown in Fig. 10(b). This microstructure suggested melting followed by slow re-solidification.

The crystal structure of the MoSi$_2$ nodules was determined by CBED analysis. Figure 12 shows the [001] zone axis CBED pattern obtained from the

MoSi$_2$ nodules. Figure 12(a) shows the zero-order Laue layer pattern which possesses 4 mm projection-diffraction symmetry; Fig. 12(b) shows the whole-pattern symmetry revealing 4 mm symmetry as well. Examination of both the [100] and [110] orientations, not shown here, displayed 2 mm whole-pattern symmetries. These symmetries, in conjunction with the 4 mm symmetry of the [001] orientation, are consistent with a point group of 4/mmm. From the whole pattern shown in Fig. 12(b) the centering of the structure was determined to be body-centered (I). Since no dynamical absences could be located in any orientations, the space group was determined to be I4/mmm. MoSi$_2$ has been reported to exist as two different crystal structures, C40 hexagonal (β-MoSi$_2$) above 1900°C and as C11$_b$ (body-centered tetragonal
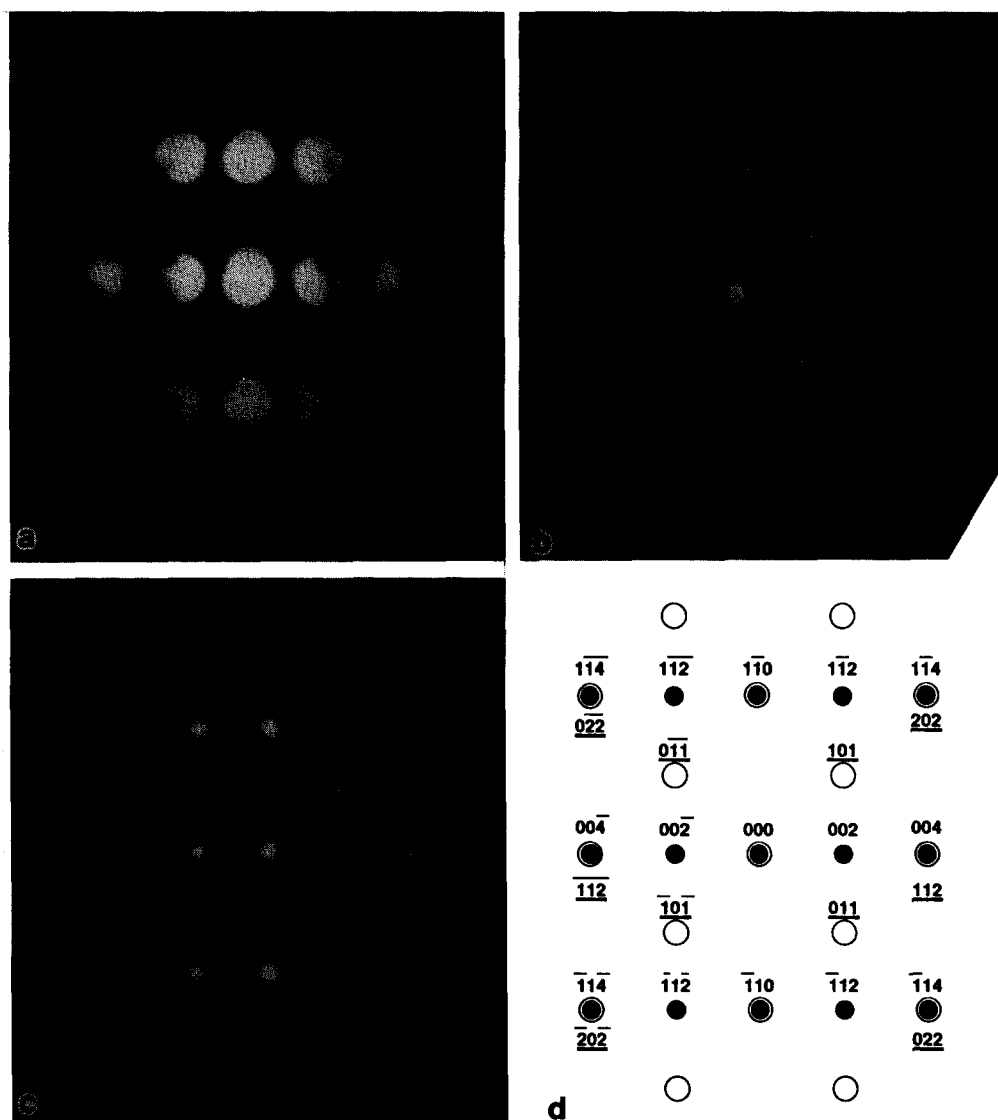

Fig. 13. (a) [110] microdiffraction pattern from one side of the twin plane in a MoSi$_2$ nodule and (b) shows a [111] selected area diffraction pattern (SADP) from the other side, (c) shows a composite SADP across both sides of the twin, and (d) shows the indexing of the composite pattern. The solid circles indicate the first variant pattern shown in (a), the open circles represent the reflections from the second variant shown in (b), and a solid circle inside an open circle indicates overlapping reflections.

α-MoSi$_2$) below 1900°C [32]. Boettinger et al. [33] have reported that pure MoSi$_2$ exists only as the C11$_b$ structure, and that the C40 is only metastable at high temperatures as a result of other solutes stabilizing this phase. In addition, they point out that in rapid liquid quenching operations, such as plasma-spraying, and we propose here for the conditions of this reaction mechanism, that "the formation of a metastable MoSi$_2$ C40 phase can occur directly from the melt if the undercooling takes the melt below the metastable melting point of the C40 phase. This melting point may be only a few degrees Celcius below the melting point of the C11$_b$ phase." The MoSi$_2$ phase observed here is consistent with the low temperature tetragonal phase (C11$_b$) suggesting that either this phase formed via solid-state below 1900°C,

in contradiction to the mechanism being proposed herein, or was formed from the liquid state (consistent with the mechanism proposed here) first as the high-temperature C40 structure which subsequently transformed during cooling to the low-temperature C11$_b$ phase.

Mitchell et al. [34] have examined the (C40) hexagonal-to-(C11$_b$) tetragonal transformation of MoSi$_2$ in plasma-sprayed processing in which the MoSi$_2$ phase starts to form in the liquid state. Their results indicate that a hexagonal-to-tetragonal phase transformation does occur in their experiments even for the very rapid solidification rates of the plasma-spray processing. During the transformation the stacking is changed from ABC in the hexagonal phase to AB in the tetragonal phase, and three different stacking
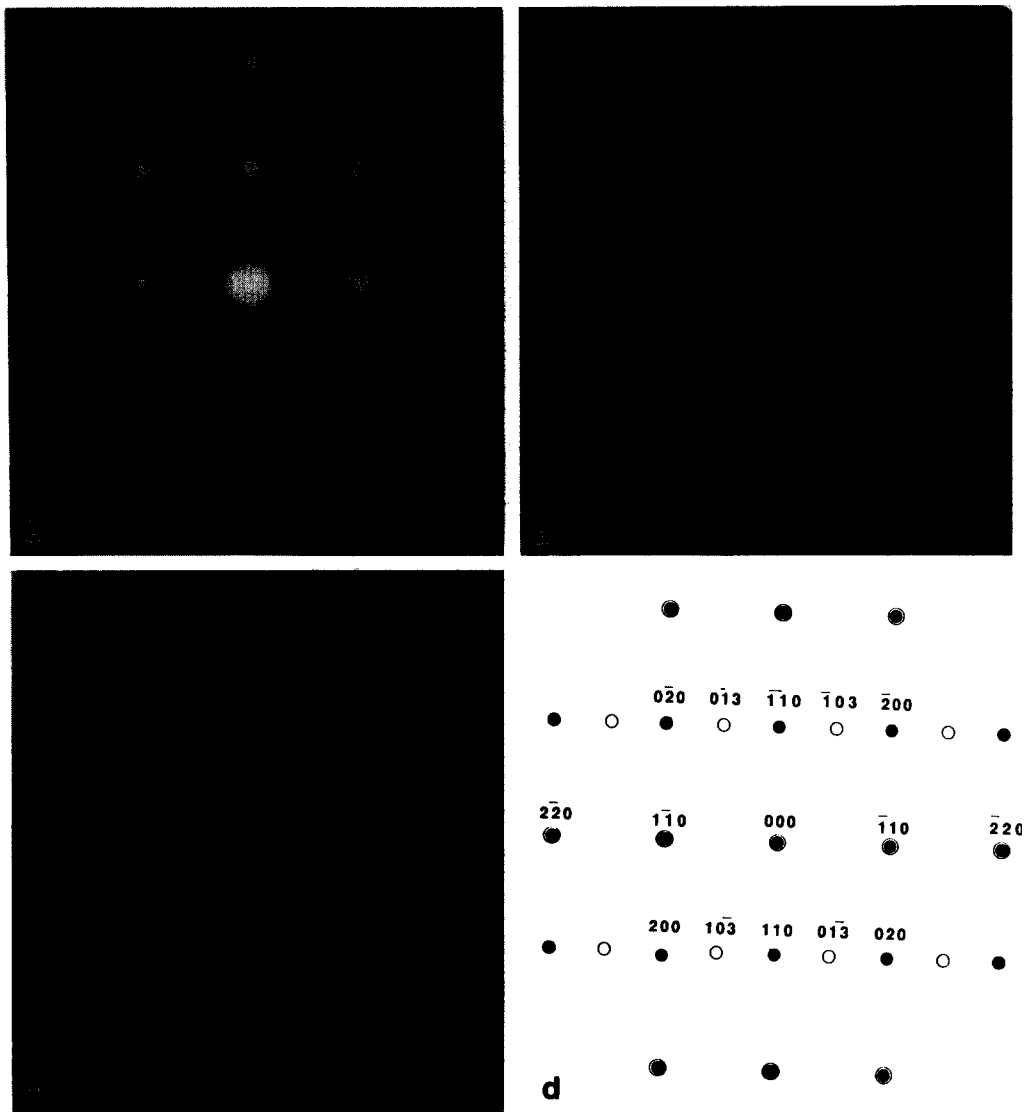

Fig. 14. (a) [001] selected area diffraction pattern from one side of the twin plane in a MoSi$_2$ nodule and (b) shows a [331] selected area diffraction pattern from the other side, (c) shows a composite SADP across both sides of the twin, and (d) shows the indexing of the composite pattern. The solid circles indicate the first variant pattern shown in (a), the open circles represent the reflections from the second variant shown in (b), and a solid circle inside an open circle indicates overlapping reflections.

variants are possible within a given hexagonal grain: AB, BC and CA. If two different variants form within a given grain they will possess a twin relationship with each other. Mitchell et al. [34] suggest that their observation of {110} twins in the tetragonal MoSi$_2$ phase is a direct consequence of the hexagonal-to-tetragonal phase transformation. Figure 11 shows a nodule of MoSi$_2$ containing a twin; each MoSi$_2$ nodule examined, when suitably oriented, displayed twins. Figure 13(a) shows a [110] microdiffraction pattern from one side of the twin plane and Fig. 13(b) shows a [111] selected area diffraction pattern (SADP) from the other side. Figure 13(c) shows a composite SADP across both sides of the twin, and Fig. 13(d) shows the indexing of the composite pattern; the twin boundary is parallel to ($1\bar{1}0$) which is common to both sides of the twin, and the (004) plane of one variant is parallel to the (112) plane of the other. The crystallographic nature of the twin was further analyzed by tilting one variant into the [001] orientation, shown in Fig. 14(a), and the other variant was oriented along the [331] axis [Fig. 14(b)]. Figure 14(c) shows the combined SADP taken across the twin in this orientation, and Fig. 14(d) shows the indexing of Fig. 14(c). The twin boundary is still parallel to ($1\bar{1}0$) and common to both variants, while (130) of one variant is parallel to ($01\bar{3}$) of the other. These results are consistent with the analysis of Mitchell et al. [34] and suggest here that the nodules of MoSi$_2$ were formed from the liquid state, solidified as hexagonal, β-MoSi$_2$ which subsequently transformed to the low-temperature, tetragonal, α-MoSi$_2$. In addition, these results are consistent with the phase equilibria discussed by Boettinger et al. [33] for MoSi$_2$, particularly with regard to the C40 to C11$_b$ polymorphic transformation.

3.2. Static synthesis (diffusion couple) experiments

The morphologies of the partially-reacted regions in the Nb–Si and Mo–Si systems have unique features that are indicative of the mechanisms operating. The profuse presence of NbSi$_2$ and MoSi$_2$ nodules at the Nb–Si and Mo–Si interfaces, and, more importantly, interspersed in the silicon are a unique aspect of shock-induced chemical reactions. In order to both compare reaction mechanisms and assess the kinetics of reaction under conventional heat treatment, in the solid state, pieces of niobium and silicon were polished flat, clamped together, and then encapsulated. These diffusion couples were annealed at 1200°C for different times, sectioned, and analyzed. Figure 15(a) shows typical reaction layers that formed as a result of solid-state diffusion (in this example the couple was annealed at 1200°C for 2 h). The interdiffusion resulted in the formation of a thick layer of NbSi$_2$, adjacent to the silicon sample, followed by a lamellar eutectic structure of Nb$_5$Si$_3$ in NbSi$_2$, growing from a layer of Nb$_5$Si$_3$ adjacent to the pure Nb sample. These reaction products and morphologies are consistent and predictable from the Nb–Si phase diagram. The

thicknesses of the product layers (excluding the eutectic region) as a function of time for each of the diffusion couples fabricated are plotted in Fig. 15(b). The data can be easily rationalized in terms of a simple diffusion equation

$$x = k\sqrt{Dt} \tag{1}$$

where x is the thickness of the reaction layer, D is the diffusion coefficient, t is the time, and k is a parameter that is a function of the geometry, phases formed, etc. The activation energy for diffusion for these materials varies from 200 to 400 kJ/mol. Taking a weighted average (among the available data) between the activation energies for self-diffusion of silicon and niobium, a value of 350 kJ/mol is obtained. Hence

$$x = KD_0^{\frac{1}{2}}(e^{-\Delta Q/RT}t)^{\frac{1}{2}}. \tag{2}$$

By grouping the two unknown parameters k and $D_0^{\frac{1}{2}}$ and fitting equation (2) to the experimental results of Fig. 15(b), it is possible to predict reaction layer thicknesses as a function of time for both Nb$_5$Si$_3$ and NbSi$_2$. These predicted thicknesses, for a range of temperatures below the melting point of silicon, are plotted in Fig. 15(c). The effect of temperature on the product layer thickness is very small, in the scale of Fig. 15(c). The usefulness of this plot is that it enables comparison of the amount of expected reaction product on the time scale of the shock experiments. The predicted reaction layer thicknesses, for a time of 5 μs (maximum duration of stress pulse within shocked specimens) and a temperature of 1673 K [the maximum admissible temperature for solid-state process (the melting temperature of silicon = 1687 K)] are 10^{-7} and 10^{-9} μm for NbSi$_2$ and Nb$_5$Si$_3$, respectively. Under shock compression, the reaction front advances by a dimension on the order of the radius of the nodules (~ 1 μm) within this same time span (5 μs). Thus, the reaction rates under shock compression are 10^7–10^9 times higher than under static, solid-solid conditions.

3.3. Proposed reaction mechanism

The analysis of the partially-reacted regions in the Nb–Si and Mo–Si shock experiments revealed the detailed nature of the reaction sequence and mechanisms (for the sake of brevity only the Nb–Si system will be discussed below, however this analysis applies equally well to the Mo–Si system). A thermodynamic treatment of the reaction mechanism proposed below is given in a companion paper [27]. The preponderance of small NbSi$_2$ particles surrounded by silicon, as well as the existence of NbSi$_2$ particles attached to the niobium particles (Figs 3 and 4) are evidence for a reaction mechanism in which the NbSi$_2$ or MoSi$_2$ particles are continuously being generated at the interface and ejected into the (molten) silicon. Thus, no permanent diffusion barrier that would slow down the reaction process is formed, and reaction can proceed at a constant rate until the entire metal
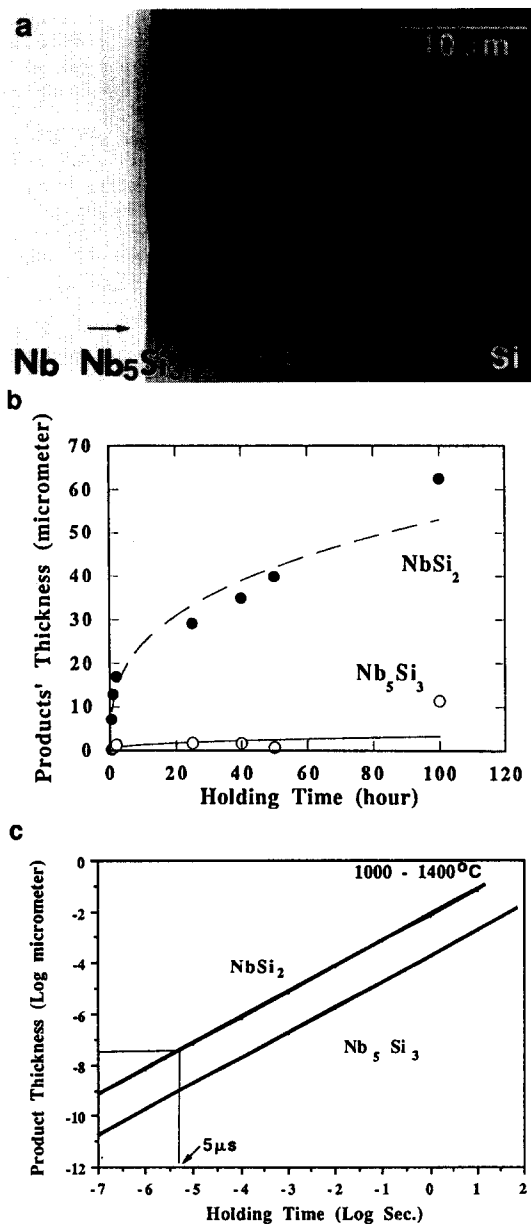
Fig. 15. (a) Backscattered electron micrograph of typical reaction layers that formed as a result of solid-state diffusion (in this example the couple was annealed at 1200°C for 2 h). The interdiffusion resulted in the formation of a thick layer of $NbSi_2$, adjacent to the silicon sample, followed by a lamellar eutectic structure of Nb_5Si_3 in $NbSi_2$, growing from a layer of Nb_5Si_3 adjacent to the pure Nb sample. (b) a plot of the measured thicknesses of the product layers (excluding the eutectic region) as a function of time for each of the diffusion couples fabricated, the dashed and solid lines represent best fit curves. (c) is a plot of the predicted thicknesses, based on equation (2), for a range of temperatures below the melting point of silicon.

(Nb or Mo) or silicon is consumed. The shock-induced reaction is initiated along the solid metal–molten Si interface. After reaction has proceeded to a certain extent, surface (interfacial) forces become dominant, and the liquid reaction product agglomerates, forming a spherule. At this point,

reaction kinetics are drastically decreased, due to the reduction in the Nb–Si interfacial area, and solidification of the disilicide sphere starts. As the sphere solidifies, new nuclei form along the Nb–Si interface. The new nuclei grow, agglomerate into spheres when they reach a critical size, and thereby form neighboring spheres. As these neighboring spheres solidify, they exert forces on the first sphere, expelling it into the molten silicon, and thus exposing fresh surfaces. This reaction process can continue unimpeded, until the reactants are consumed. In addition, turbulent flow of the liquid silicon under shock can also contribute to the detachment of the spherules from the interface. The companion paper (Part II; [27]) presents this mechanism in detail.

4. CONCLUSIONS

1. It was possible to successfully initiate and propagate shock-induced reactions for the two systems investigated (Nb–Si and Mo–Si), and the extent of reaction was found to increase with shock energy, shock temperature, and the energy of reaction.

2. The following qualitative statements can be made: (a) as the heat of reaction increases, the shock pressure/temperature necessary for full reaction decreases, and (b) the extent of shock-induced reaction increases with shock energy, at a constant temperature, and with temperature, at a constant shock energy.

3. Electron microscopy observations reveal that the main reaction product in the partially-reacted regions is the disilicide formed from the molten state as spherules with radii of approx. 1–2 μm. These spherules are formed at the metal–Si interface and are expelled into the silicon.

4. There is clear indication that silicon melting is a prerequisite for shock-induced reactions.

5. The kinetics in static solid-state reactions were established and found to be lower, by $\sim 10^8$ compared to the kinetics in shock compression.

6. A reaction mechanism under shock compression for the metal–Si interface is proposed involving the dissolution of Nb or Mo into molten Si, producing the molten intermetallic, with its subsequent spheroidization, solidification, and expulsion into the surrounding liquid silicon melt. In this reaction mechanism a fresh solid (Nb or Mo)–liquid (Si) interface is continuously maintained, enabling a high reaction rate.

REFERENCES

1. S. S. Batsanov, A. A. Deribas, E. V. Dulepov, M. G. Ermakov, and V. M. Kudinov, *Combust. Explos. Shock Waves (USSR)*1, 47 (1965).
2. Y. Horiguchu and Y. Nomura, *Carbon* 2, 436 (1965).
3. Y. Horiguchu and Y. Nomura, *Chem. Inds, Lond.*, p. 1791 (1965).
4. G. A. Adadurov, V. I. Gold'anskii, and P. A. Yampol'skii, *Mandeleev Chem. J.* 18, 92 (1973).
5. G. A. Adadurov, and V. I. Gold'anskii, *Russ. chem. Revs* 50, 948 (1981).
6. A. N. Dremin and O. N. Breusov, *Russ. chem. Revs* 37, 392 (1968).
7. S. S. Batsanov, *Russ. chem. Revs* 37, 197 (1968).
8. S. S. Batsanov, G. S. Doronin, S. V. Klochdov and A. I. Tent, *Combust. Explos. Shock Waves* (USSR) 22, 765 (1986).
9. R. Graham, B. Morosin, E. L. Venturini and M. J. Carr, *Ann. Rev. Mater. Sci.* 16, 315 (1986).
10. W. F. Hammetter, R. A. Graham, B. Morosin, and Y. Horie, in *Shock Waves in Condensed Matter* (edited by S. C. Schmidt and N. C. Holmes), p. 431. Elsevier Science, Amsterdam (1988).
11. B. Morosin, R. A. Graham, E. L. Venturini, M. J. Carr and D. L. Williamson, in *Shock Waves in Condensed Matter* (edited by S. C. Schmidt and N. C. Holmes), p. 435. Elsevier Science, Amsterdam (1988).
12. B. R. Krueger and T. Vreeland Jr, in *Shock-Wave and High-Strain-Rate Phenomena in Materials* (edited by M. A. Meyers, L. E. Murr and K. P. Staudhammer), p. 245. Marcel Dekker, New York (1992).
13. B. Krueger, A. Mutz and T. Vreeland Jr, *Metall. Trans.* 23A, 55 (1991).
14. Y. Horie, R. A. Graham, and I. K. Simonsen, *Mater. Lett.* 3, 354 (1985).
15. Y. Horie and M. J. Kipp, *J. appl. Phys.* 63, 5718 (1988).
16. M. B. Boslough, *J. chem. Phys.* 92, 1839 (1990).
17. Z. Iqbal, N. N. Thadhani, N. Chawla, B. L. Ramakrishna, R. Sharma, S. Skumeyev, F. Reidinger and H. Eckhardt, *Appl. Phys. Lett.* 55, 2339 (1989).
18. N. N. Thadhani, A. Advani, I. Song, E. Dunbar, A. Grebe and R. A. Graham, in *Shock-Wave and High-Strain-Rate Phenomena in Materials* (edited by M. A. Meyers, L. E. Murr and K. P. Staudhammer), p. 271. Marcel Dekker, New York (1992).
19. L. H. Yu and M. A. Meyers, *J. Mater. Sci.* 26, 601 (1991).
20. M. A. Meyers, L. H. Yu and K. S. Vecchio, in *Shock Compression of Condensed Matter—1991*, (edited by S. C. Schmidt, R. D. Dick, J. W. Forbes and D. G. Tasker), p. 629. North Holland, Amsterdam (1992).
21. C. S. Smith, *Trans. Am. Inst. Min. Engrs* 212, 574 (1958).
22. E. Hornbogen, *Trans. Am. Inst. Min. Engrs* 221, 721 (1961).
23. M. A. Meyers, *Scripta metall.* 12, 21 (1978).
24. J. Weertman, in *Shock-Wave and High-Strain-Rate Phenomena in Metals* (edited by M. A. Meyers and L. E. Murr), p. 469. Plenum Press, New York (1981).
25. W. Gourdin, *J. appl. Phys.* 55, 172 (1984).
26. R. B. Schwarz, P. Kasiraj, T. Vreeland Jr, and T. J. Ahrens, *Acta metall.* 32, 1243 (1984).
27. M. A. Meyers, L.-H. Yu and K. S. Vecchio, *Acta metall. mater.* 42, 715 (1994).
28. A. B. Sawaoka and T. Akashi, U. S. Patent 4655830 (1987).
29. F. R. Norwood and R. A. Graham, in *Shock-Wave and High-Strain-Rate Phenomena in Materials*, p. 989. Marcel Dekker, New York (1992).
30. R. P. Elliot and F. A. Shunk (contributing editors), *Bull. Alloy Phase Diagr.* 2, (1981).
31. B. F. Buxton, J. A. Eades, J. W. Steeds and G. M. Rackman, *Phil. Trans. R. Soc.* 281, A1301, 171 (1976).
32. P. Villars, *Pearson's Handbook of Crystallographic Data for Intermetallic Phases* (edited by P. Villars and L. D. Calvert), Am. Soc. Metals, Metals Park, Ohio (1985).
33. W. J. Boettinger, J. H. Perepezko and P. S. Frankwicz, *Mater. Sci. Eng.* A155, 33 (1992).
34. T. E. Mitchell, R. G. Castro and M. M. Chadwick, *Phil. Mag.* A65, 1339 (1992).